Contents lists available at ScienceDirect

Applied Catalysis B: Environment and Energy

Tuning CO_2 photoreduction: CoN/KPCN catalysts for High CH_4 selectivity through an efficient microwave molten salt heating synthesis

Suxin Qiu , Honglei Shao , Chengpeng He , Xueling Song , Jinchen Fan , Yuhua Xue , Guisheng Li , Shuning Xiao [*]

School of Materials and Chemistry, University of Shanghai for Science and Technology, Shanghai 200093, China

ABSTRACT

Photocatalytic reduction of CO_2 to CH_4 holds promise for sustainable energy and CO_2 mitigation. In this study, we present the rapid synthesis of efficient composite photocatalysts via a one-step microwave molten salt heating method. Typically, potassium ions (K^+) are directionally doped into polymeric carbon nitride (PCN) interlayer cavities, while CoN nanoparticles selectively form on K-doped PCN (KPCN). CoN/KPCN catalysts exhibit exceptional photocatalytic performance, yielding 45.71 μmol g^{-1} h^{-1} CH_4 with 98.18% selectivity under visible light illumination. This mainly results from the synergistic effect of the enhanced crystallinity, expanded light absorption, efficient charge transfer, superior CO_2 adsorption, and enhanced carrier dynamics. More importantly, the introduction of K^+ is in favor of the high CH_4 photoreduction selectivity both in view of kinetically and thermodynamically. This study informs carbon nitride-based photocatalyst development and underscores the potential of CoN/KPCN as a catalyst for high CH_4 selectivity in CO_2 photoreduction, contributing to sustainable energy and environmental conservation.

1. Introduction

The issue of global warming has attracted more and more attention, primarily originating from the excessive emission of greenhouse gases, particularly carbon dioxide (CO_2) [1–4]. Inspired by the natural photocatalysis, photocatalytic CO_2 reduction has been regarded as an eco-friendly and efficient technology to acquire high-value-added chemicals, playing a pivotal role in advancing sustainable development and achieving carbon neutrality [5–7]. Until now, a various of photocatalysts, including TiO_2, CuO, CeO_2 CdS, and ZnS have been reported. The photocatalytic efficiency and selectivity of products are still two bottleneck problems. Therefore, the well-design and construction of efficient photocatalysts is still a critical step in the process of CO_2 photoreduction [8,9].

Polymeric carbon nitride (PCN), as a metal-free polymeric semiconductor, has received much attention in the field of photocatalysis due to its non-toxicity, low-cost, suitable bandgap and visible-light response [10]. Nonetheless, its small specific surface area and low crystallinity have led to PCN with low CO_2 adsorption capacity and high carrier recombination rate, largely hindering the further enhancement of photocatalytic performance [11–13]. To overcome the above limitations, many effective modification strategies for PCN have been explored.

Notably, the construction of PCN-based heterojunctions was also regarded as an efficient strategy to improve the separation efficiency and the photocatalytic activity of the initial carbon nitride [14,15]. For example, Geng et al. created a 2D/2D α-Fe_2O_3/g-C_3N_4 Z-scheme heterojunction exhibiting strong visible light absorption ability, remarkable charge separation and transfer capabilities, a high interface area, and widely dispersed active sites [16]. Li et al. synthesized a CZS/PCN S-scheme heterojunction composite by one-pot direct annealing, resulting in a larger specific surface area and improved carrier separation and transfer efficiency [17]. Moreover, transition metal compounds are usually applied as efficient co-catalysts to construct heterojunctions with carbon nitride, such as WO_3/PCN, CoO/PCN, CeO_2/PCN and TiO_2/PCN [18–21].

Cobalt nitride (CoN) with metal-like properties exhibits highly efficient electrical conductivity [22,23]. When applied as a cocatalyst, CoN can efficiently transfer photogenerated electrons to participate in redox reactions for enhancing the photocatalytic activity of composite catalysts. Di et al. reported that the loading of Co_2N on the surface of BiOBr induces a strong electronic interaction between their interface, facilitating the electron transfer from BiOBr to Co_2N. Meanwhile, the

introduction of Co_2N reduces the activation energy barrier for the *COOH formation in the rate-limiting step, promoting CO_2 activation and reduction [24]. Similarly, Gong et al. prepared $Mn_{0.2}Cd_{0.8}S/CoN$ composite photocatalysts via electrostatic self-assembly process, leading to the spontaneous directional transfer of photogenerated carriers from $Mn_{0.2}Cd_{0.8}S$ to CoN. This transfer greatly suppressed carrier recombination and improved the separation and transfer rate of carriers [25].

Additionally, the molten salt method is widely applied to improve the crystallinity of PCN photocatalysts [26]. The molten salts (such as KBr, KCl, NaCl, LiCl) are beneficial to uniformly thermally condensation of precursor materials for the synthesis of PCN catalysts with high crystallinity [27–29]. Furthermore, the alkali metals (such as K, Na, Li) are easily infiltrated into the crystalline structure of PCN during the thermal condensation process for adjusting the electronic structure. Dong et al. synthesized CN-K catalysts with a unique electronic structure using molten salt (KBr) and thiourea as precursors [30]. K^+, presented in the interlayer positions of the PCN, leads to the extension of the π-conjugated system, and a drastic rearrangement of the PCN layers, resulting in the electron loss of in the sp^2 orbital plane and the electron accumulation of in the p_z orbital plane. Moreover, K provides a rapid channel for charge transfer, thereby promoting the separation and transfer of photogenerated carriers. Xu et al. employed KCl as a structure inducer, with K^+ acting as intelligent "binder" for rearranging the structure of amorphous polymer carbon nitride [31]. Furthermore, Zhang et al. utilized molten potassium salt (KCl/KOH) to prepare K-CN with improved crystallinity and enhanced charge transport capacity. This enhancement resulted from the "sewing" and "cutting" role of alkaline potassium salt during polymerization [32].

Compared with the traditional resistance heating method, microwave-assisted heating has been widely used in the field of nanomaterials preparation by virtue of its short reaction time, high reaction rate, and good selectivity [33–35]. It has also become an effective means of modifying carbon nitride [36,37]. When microwave irradiation acts on the molten salt rich in ionic conductors, it can cause the ionic conductors to be orderly arranged and undergo violent reciprocating motions at an ultra-high frequency rate of billions of times per second. In this process, the mobility of the ionic conductors is significantly enhanced, which not only contributes to the formation of stable and uniform ionic liquid heating conditions, but also promotes the rapid nucleation and growth of crystals, thus improving the crystallinity and homogeneity of carbon nitride [38]. For example, Yu et al. obtained highly crystallized $g-C_3N_4$ photocatalysts prepared by using microwave-assisted heating in just a few minutes [39]. Meanwhile, a significant heating effect will be formed from the inside out during the violent collision of ions, while the tanδ (loss angle tangent, which indicates the wave exothermic capacity of dielectric materials) of the ionic conductor will increase dramatically as the temperature rises, which further enhances the wave-absorbing capacity of the ionic conductor and forms a positive feedback effect [40]. In addition, microwaves also could realize selective heating of transition metal elements, thus promoting the generation of transition metal compounds. Notably, in situ synthesis of composite catalysts via microwave heating mechanism has been shown to be an effective strategy for modifying catalysts [41,42].

In this study, we employed the microwave molten salt method to rapidly construct CoN/KPCN composite photocatalysts. The in situ loading metallic CoN and the introduction of alkali metal K were achieved simultaneously. The formation of Schottky junctions between CoN and KPCN facilitates the spontaneous flow of photogenerated carriers from KPCN to CoN, verified by experiments and DFT calculations. The effective inhibition of carrier recombination accelerates carrier separation and transfer. More importantly, the loading of CoN significantly enhances CO_2 adsorption while providing more reaction sites. The resulting CoN/KPCN composite catalyst possesses a more negative conduction band position, favoring the CO_2 photoreduction reaction. The introduction of alkali metal K widens the visible light absorption and provides additional electrons for the reduction process, ultimately promoting the protonation of the intermediate product *CO to form *CHO. Under AM 1.5 G simulated illumination, CoN/KPCN shows a significantly enhanced CO_2 reduction to CH_4 activity of 45.71 μmol g^{-1} h^{-1} and high selectivity of CH_4 of 98.18%. This research demonstrates a promising approach to enhancing the efficiency of carbon nitride-based photocatalysts for CO_2 reduction.

2. Experimental section

2.1. Preparation of PCN and KPCN

The catalysts were synthesized using a one-step microwave thermal polymerization method with the following procedure: 5 g of urea was uniformly ground in an agate mortar and then transferred to a 25 mL alumina crucible with a cover. This crucible was placed in a microwave muffle furnace (CY-AS1200C-S, HUAEMW Co., Ltd.) and heated to 550 °C at a rate of 10 °C/min for 1 h. After cooling to room temperature, the resulting powder was thoroughly washed with deionized water (DI water) and ethanol. After centrifugation, it was dried in a blast drying oven at 60 °C for 12 h, yielding a pale-yellow powder product known as PCN.

For the preparation of KPCN, the same process was followed, with the only difference being the addition of 200 mg KBr to the precursor mixture. This variation resulted in the formation of a yellow solid powder product, which was named KPCN.

2.2. Preparation of CoN/KPCN

$Co(NO_3)_2 \cdot 6 H_2O$ was incorporated into the process. Similar to the synthesis of PCN and KPCN, the precursors, including 5 g of urea, 200 mg of KBr, and $Co(NO_3)_2 \cdot 6 H_2O$ were milled under an infrared lamp. This process yielded yellow-gray powdery products, designated as CoN/KPCN-x, where x represents the mass of $Co(NO_3)_2 \cdot 6 H_2O$ (x = 6.25, 12.50, 18.75, 25.00, 31.25, and 37.50, in mg). From this point forward, we will refer to CoN/KPCN-25.00 as CoN/KPCN in subsequent sections.

2.3. Characterization

The crystal structure and phase composition of catalysts were characterized by an X-ray diffractometer (XRD, Bruker D8 ADVANCE, Japan) using Cu Kα as the radiation source (λ = 1.54 Å) with a 2θ scanning speed of 2°/min and a 2θ range of 5–80°. The morphology of catalysts was recorded by field-emission scanning electron microscopy (SEM, FEI Quanta FEG) with energy-dispersive spectra (EDS) mapping. The transmission electron microscope (TEM) and high-resolution transmission electron microscopy (HRTEM) image were recorded by FEI Tecnai G2 F30. The bandgap of the catalysts was analyzed by a UV–vis diffuse reflectance spectroscopy (UV–vis DRS, Shimadzu UV-2600, Japan) equipped with an integrating sphere, applying $BaSO_4$ as the standard reference. Fourier transform infrared spectra (FTIR) were measured by a PerkinElmer Spectrum 100 spectrophotometer with KBr as the standard reference. The surface electronic states of catalysts were analyzed by X-ray photoelectron spectroscopy (XPS, Thermo Scientific K-Alpha). All binding energies were referenced to the C1s peak of 284.8 eV. Steady-state fluorescence (PL) and time-resolved fluorescence (TRPL) emission spectra were recorded on a fluorescence spectrophotometer (Edinburgh instruments, F-7100) at room temperature. The Brunauer−Emmett−Teller (BET) surface area (SBET) and pore size distribution were determined using a Micromeritics ASAP 2000 nitrogen adsorption apparatus. CO_2 adsorption isotherms are measured by a BELSORP-max setup.

2.4. Gas-solid phase photocatalytic CO_2 reduction

The gas-solid photocatalytic CO_2 reduction was conducted within a sealed quartz glass reactor at ambient temperature, without the use of

any sacrificial agents or co-catalyst. Initially, 20 mg of catalysts were dispersed in 20 mL of DI water within the quartz reactor through ultrasonication. The reactor was then transferred to an oven and dried at 60 °C. As the water completely evaporated, the catalyst settled at the bottom of the reactor, forming a uniform photocatalytic layer. Following this, the reactor was sealed, and a stream of N_2 was passed through it for 30 min after adding 0.084 g of sodium bicarbonate ($NaHCO_3$) into the groove of the reactor. Subsequently, 300 μL of H_2SO_4 (aq, 2 M) was injected into the tank to react with $NaHCO_3$, generating CO_2 and H_2O vapors for photocatalytic CO_2 reduction process. The quartz reactor was then positioned beneath a 300 W Xe light source (PLS-SXE 300D, Beijing Perfectlight Technology Co., Ltd.) equipped with an AM 1.5 G cut-off filter. The distance between the photocatalyst and the light source was maintained at approximately 10 cm. After 1 h of illumination, the reactor was connected to a gas chromatograph (A91 Plus, Panna) to analyze the gas composition.

2.5. Photoelectrochemical measurements

The photoelectrochemical properties of the catalysts were assessed using a standard three-electrode system, with a 0.5 M Na_2SO_4 aqueous solution serving as the electrolyte at CHI660E electrochemical workstation. To evaluate photochemical activity, 5 mg of photocatalysts were dispersed in a mixture consisting of 20 μL of Nafion (5 wt%) solution and 980 μL of solvent ($V_{isopropanol}$: $V_{DI\ water}$ = 7:3), followed by ultrasonic for 30 min. Subsequently, 200 μL of the above solution was deposited onto the glassy carbon electrode (GCE) and allowed to dry naturally in a fume hood to create the working electrode. An Ag/AgCl electrode (saturated KCl solution) and a platinum plate were employed as the reference electrode and the counter electrode, respectively. Under illumination of a 300 W Xe lamp (with an AM 1.5 G filter), the photocurrent-time curves were recorded with a bias voltage of 0.4 V vs. Ag/AgCl by turning on and off the lamp every 60 s. The electrochemical impedance spectra (EIS) were measured under open-circuit voltage conditions, with a frequency range of 0.01 Hz to $1 * 10^6$ Hz and an AC amplitude of 10 mV.

2.6. Density functional theory (DFT) calculations

The computational aspect of this study employed periodic density functional theory (DFT) using the VASP (Vienna Ab-initio Simulation Package) [43]. The exchange and correlation energy were evaluated within the generalized gradient approximation (GGA) using the PBE functional [44]. The electronic self-consistent energy convergence accuracy (EDIFF) was set as 1×10^{-4} eV, and a 520 eV plane-wave cutoff was applied.

The adsorption energy (E_{ads}) was calculated using the following formula:

$$E_{ads} = E_{total} - (E_{slab} + E_{gas})$$

Here, E_{total} represents energy of the entire system, including the substrate and adsorbed gas, E_{slab} is the energy of single substrate, and E_{gas} is the energy of isolated gas molecule (in this case, oxygen). The DFT-D dispersion correction function (IVDW=11) was applied account for non-bonding interactions, such as Van der Waals forces.

The change of Gibbs free energy (ΔG) for each reaction step is given as follows:

$$\Delta G = \Delta E + \Delta ZPE - T\Delta S$$

Where ΔE represents the total energy difference between the product and reactant, which can be directly obtained from DFT calculations. ΔZPE and $T\Delta S$ are the zero-point energy correction and the entropy change at room temperature (298.15 K), respectively.

3. Results and discussion

3.1. Morphology and microstructural characterization

The morphology and microstructure of PCN, KPCN, and CoN/KPCN were characterized through scanning electron microscopy (SEM), transmission electron microscope (TEM), and high-resolution transmission electron microscopy (HRTEM). As presented in Fig. 1, all catalysts exhibited wrinkled lamellar particles with diameter of a few microns, consisting of irregular nanosheet layers. Upon introducing K and CoN, the nanosheets of PCN thickened, and the surface became progressively rougher, especially in CoN/KPCN. TEM and HRTEM further confirmed the irregular lamellar structure of PCN (Fig. S1) and CoN/KPCN as illustrated in Fig. 2a-b. For the composite catalyst CoN/KPCN, CoN nanoparticles were selectively attached to the surface of KPCN. HRTEM revealed obvious lattice fringes, as described in Fig. 2c. Further analysis revealed that lattice stripes with d= 1.091 nm originated from the (110) crystal plane of KPCN, while d= 0.248 nm corresponded to the (111) crystal plane of CoN. In contrast, PCN exhibited no observable lattice fringes in the HRTEM image (Fig. S1d). These results confirm the successful loading of CoN onto the surface of KPCN. Similarly, the diffraction spots of KPCN and CoN are displayed in the SAED pattern (Fig. 2d), further confirming the successful recombination of CoN and KPCN. EDS mapping diagram (Fig. 2e-i) show the uniform distribution of C, N, K, Co, and O elements in CoN/KPCN.

The crystal structure of the prepared catalysts was studied using X-ray diffraction (XRD). As shown in Fig. 3a, PCN exhibits two typical diffraction peaks: the (100) facet at 12.98° and the (002) facet at 27.51°, corresponding to the repeated tri-s-triazine (heptazine) units and the stacking of the conjugated aromatic system of graphitic layered materials [45,46]. Upon introducing K, the diffraction peak at 12.98° disappeared, replaced by two new diffraction peaks near 8.17° and 10.20°, corresponding to the intrinsic (110) and (020) facets of KPCN, with the crystal lattice distances about 1.091 and 0.874 nm, respectively [31]. In CoN/KPCN-x, two new diffraction peaks at 36.18° and 42.19° emerged, attributed to CoN (111) facet and (200) facet [25]. These results demonstrate the successful doping of K into the PCN lattice and confirm the in-situ complexation of KPCN with CoN. Moreover, compared to PCN, the 2θ angle of the (002) crystal facet shifted to a higher angle for KPCN and CoN/KPCN, implying that K entered the interlayers of PCN under microwave condition, reducing the layer spacing and improving crystallinity.

Fourier transform infrared spectroscopy (FTIR) revealed the surface functional groups on the catalysts. As shown in Fig. 3b, for PCN, fingerprint signals in the 1200 to 1700 cm^{-1} range were attributed to the typical stretching and bending vibration modes of C=N and C–N in the triazine rings. Peaks at 809 cm^{-1} and 890 cm^{-1} corresponded to the typical out-of-plane bending vibration of the heptazine rings and the characteristic peak of the C-N vibration [47]. These peaks persisted in KPCN and CoN/KPCN, indicating that the main chemical structure of PCN remained intact [48]. Additionally, KPCN and CoN/KPCN presented a new peak at 2180 cm^{-1}, belonging to the asymmetric stretching modes of the cyano groups (C≡N), potentially due to the decomposition or incomplete polymerization of part of the heptazine structure resulting from the creation of localized high-temperature by the molten salts under microwave action [49]. Cyano groups strongly absorb electrons, creating a localized built-in electric field that enhances electron-hole pair separation [50]. The signal at 998 cm^{-1} corresponded to the symmetric vibration of metal-NC_2 (M-NC_2), suggesting that K^+ in KPCN was connected to the melon chain (-NC_2) of PCN [51]. Combined with the XRD results, it is hypothesized that K occupied the interlayer cavities of PCN, acting as a charge transfer channel to facilitate carrier passage in KPCN. Notably, the characteristic signal of Co-N bond was not detected in FTIR spectrum, likely due to the low CoN content.

To analyze the electronic interactions and valence states of the elements in catalysts, the X-ray photoelectron spectroscopy (XPS)
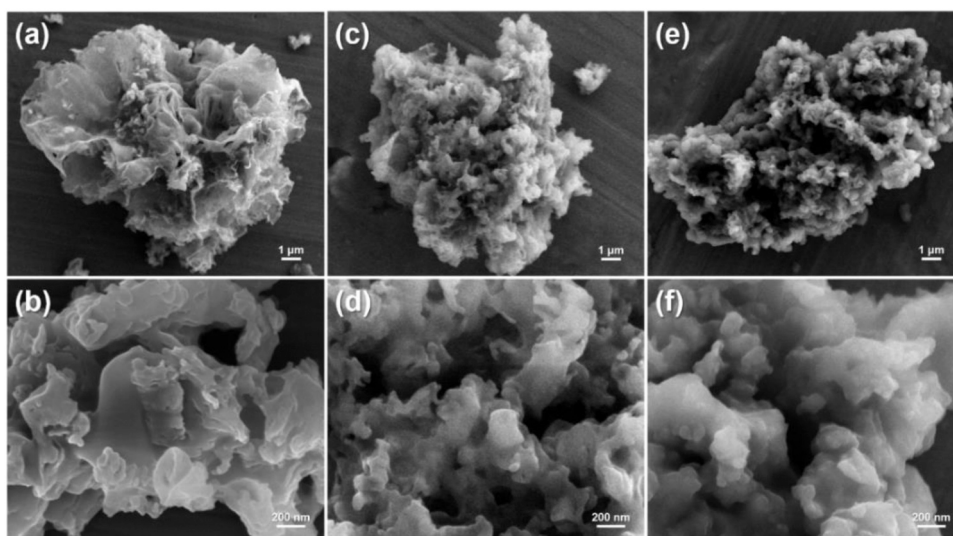
Fig. 1. SEM images of (a-b) PCN, (c-d) KPCN and (e-f) CoN/KPCN.
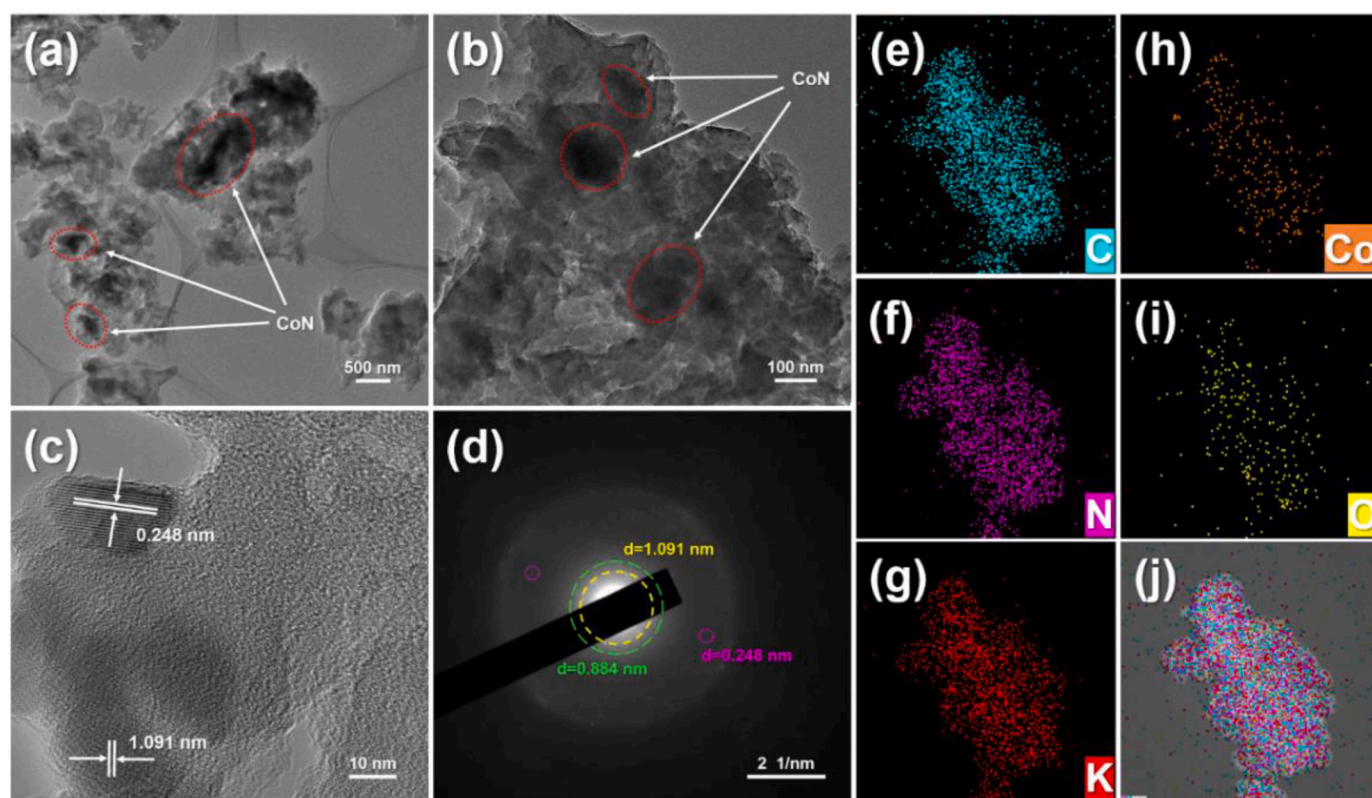

Fig. 2. TEM images (a-b), HRTEM image (c), SAED pattern (d) and EDS mapping (e-j) of CoN/KPCN.

measurements were conducted. XPS survey spectra (Fig. S2) confirmed the presence of C N, K, O elements in KPCN, and only C, N, O elements in PCN, indicating successful K doping into PCN. In CoN/KPCN, C, N, K, Co, and O elements were detected. As shown in Fig. 3c, in the C 1 s spectrum, PCN exhibited two peaks, located at 284.8 eV and 288.2 eV, assigned to graphitic C-C bonds and N-C≡N bonds. In KPCN and CoN/KPCN, the peak at 286.7 eV was attributed to C≡N, consistent with FTIR analysis. In the N 1 s spectrum (Fig. 3d), three peaks at binding energies, at 398.8 eV, 400.2 eV, and 401.2 eV were observed. The first peak at 398.8 eV derived from sp^2 N in the triazine rings, the next two peaks at 400.2 eV and 401.2 eV corresponded to bridged nitrogen atoms N-(C)₃

in the heptazine unit and amino functional groups -NHₓ, respectively [49,51]. The introduction of K shifted the binding energies of N-C≡N and C≡N to lower values, and N-(C)₃ to higher, indicating electron transfer from K to N and then to C (more details in Table S1). This suggests that K can provide electrons to PCN [30]. In the K 2p spectrum in Fig. 3e, both KPCN and CoN/KPCN displayed two peaks at 792.9 eV and 796.7 eV assigned to K $2p^{3/2}$ the latter as K $2p^{1/2}$. Furthermore, those two peaks were distinct from those for metallic K (294.7 eV) and kept a 2.8 eV doublet separation energy both in KPCN and CoN/KPCN, confirming that K existed in ion form in KPCN and CoN/KPCN[32,52]. The Co 2p spectrum exhibited four peaks (Fig. 3e), with 780.9 eV and
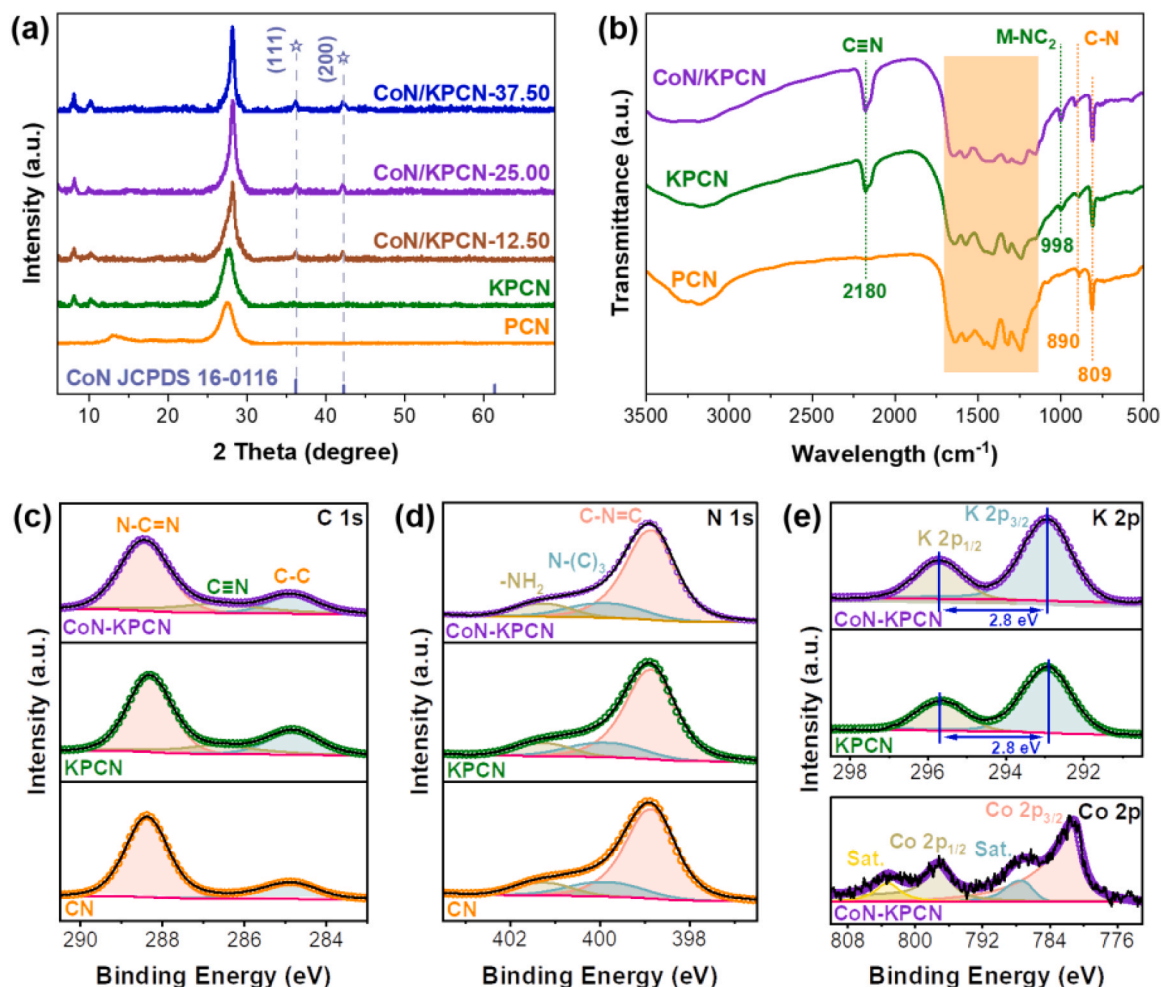
Fig. 3. XRD patterns (a) of PCN, KPCN and CoN/KPCN-x; FTIR spectra (b) of PCN, KPCN, and CoN/KPCN; XPS spectra of (a) C 1 s, (b) N 1 s, (e) K 2p and Co 2p.

796.7 eV corresponding to Co $2p^{3/2}$ and Co $2p^{1/2}$, while 786.7 eV and 803.1 eV were the satellite peaks. The Co $2p^{3/2}$ peak appeared between Co^{2+} (779.9 eV) and Co^{3+} (781.6 eV), indicating the valence state of Co between +2 and +3 in CoN/KPCN [53,54]. Comparing CoN/KPCN with KPCN, the binding energy of N-C=N, C-N = C and N-(C)$_3$ shifted, suggesting charge transfer and the formation of a built-in electric field between CoN and KPCN.

3.2. Photocatalytic CO$_2$ reduction performance

The photocatalytic CO$_2$ reduction performance of PCN, KPCN, and CoN/KPCN was evaluated under AM 1.5 G illumination using a gas-solid reaction model. Fig. 4a illustrates the presence of both CO and CH$_4$ in the photocatalytic reduction of CO$_2$ with all prepared catalysts. PCN exhibited CH$_4$ and CO yield of 1.27 µmol g^{-1} h^{-1} and 5.79 µmol g^{-1} h^{-1}, respectively with a selectivity of 46.73% for CH$_4$ and 53.27% for CO. This indicates that for PCN, the CO$_2$ photocatalytic reduction selectivity is towards CO. For KPCN, the yields changed to 8.22 µmol g^{-1} h^{-1} and 1.8 µmol g^{-1} h^{-1}, with a selectivity of 94.81% for CH$_4$ and is 5.19% for CO. Notably, the introduction of K altered the selectivity from CO to CH$_4$. In gas-solid CO$_2$ reduction, CO formation is a 2-electron pathway, while CH$_4$ formation of is an 8-electron process. The change in selectivity is attributed to the introduction of K, which enhances the photocatalytic reaction by providing more electrons at the kinetic level. When CoN was combined with KPCN, the CH$_4$ yield significantly increased to 45.71 µmol g^{-1} h^{-1}, with a selectivity of 98.18%. Performance further improved with increasing CoN content (Fig. 4b). The composite catalyst

showed optimal performance when the Co(NO$_3$)$_2$·6 H$_2$O content was 25 mg, yielding 36.0 times and 2.1 times more than those of PCN for yield and selectivity, respectively. However, excess CoN hindered CO$_2$ reduction, possibly by blocking active sites. Moreover, we summarized the photoreduction CO$_2$ performance of other catalysts in the gas-solid phase for comparison, as shown in Table S2. Stability is a key indicator of catalyst reliability. Stability is a major indicator for judging the reliability of catalysts. After seven cycles photocatalytic reactions, CoN/KPCN showed good cyclic stability with only a 15% decrease in CH$_4$ production (Fig. 4c). As shown in Fig. Fig. S3 and Fig. Fig. S4, the XRD and SEM of the catalysts before and after the reaction were in agreement, indicating that the catalysts after photoreduction were able to maintain the original structure and morphology, which further proved the stability of the prepared catalysts. To confirm that the change in selectivity resulted from K introduction, CoN/PCN was prepared following the same method used for CoN/KPCN-x, excluding KBr addition. Fig. S5 illustrated that CoN/PCN-x mainly produced CO rather than CH$_4$, confirming that the change in selectivity is due to the introduction of K. To determine the source of carbon in CO$_2$ reduction products, isotope tracing tests were performed using NaH^{13}CO$_3$ instead of NaHCO$_3$ to provide ^{13}CO$_2$ for photocatalytic experiments. Gas collected from the reactor was examined using gas chromatography-mass spectrometry (GCMS-QP2010 Plus). As shown in Fig. 4d, characteristic signals of $m/z = 17$ (^{13}CH$_4$), $m/z = 29$ (^{13}CO), $m/z = 45$ (^{13}CO$_2$) were detected, confirming that the carbon in CH$_4$ and CO products originated from CO$_2$ in the photocatalytic reaction, not from the prepared catalysts. The product selectivity was calculated using Eqs. 1 and 2:
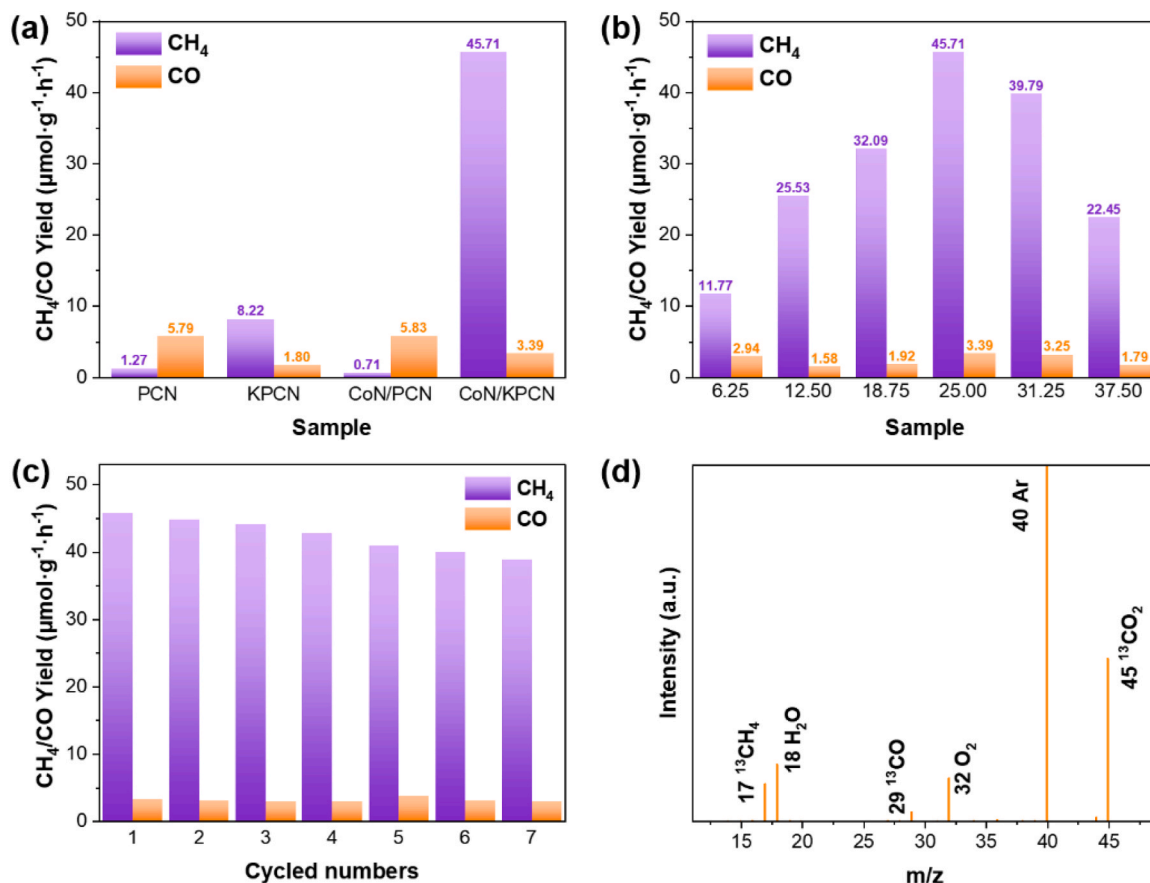
Fig. 4. Photocatalytic activity (a) CO and CH_4 yield of different samples under visible light and (b) CoN/KPCN-x, x represents the mass of Co(NO₃)₂·6 H₂O; Recycling performances (c) of Co and CH_4 production for CoN/KPCN; GC-MS spectrum (d) of the gas-phase products for CoN/KPCN in the photocatalytic reduction of $^{13}CO_2$.

$$S_{CH_4} = \frac{8 \times Y_{CH_4}}{8 \times Y_{CH_4} + 2 \times Y_{CO}} \tag{1}$$

$$S_{CO} = \frac{2 \times Y_{CO}}{8 \times Y_{CH_4} + 2 \times Y_{CO}} \tag{2}$$

3.3. Photophysical properties of photocatalysts

To understand the improved performance of photocatalytic reduction of CO_2 in the CoN/KPCN series, we examined the photoelectric properties of the synthesized catalysts. The energy band structures were determined through UV-Vis diffuse reflectance and X-ray photoelectron valence band spectrum. As seen in Fig. 5a, PCN exhibits a characteristic absorption edge at 450 nm, attributed to intrinsic band gap transition [55]. Both KPCN and CoN/KPCN show red-shifted absorption edges at 470 nm and 475 nm, respectively, indicating changes in PCN's energy band structure upon introducing K. Specifically, electrons in the outer-most layer of K are transferred to PCN, forming K^+ ions and interacting with the nearest N atoms around the cavities through a static coulomb interaction. UV-Vis DRS of the CoN/KPCN-x (Fig. S6) reveals almost identical absorption edges. Notably, excessive CoN causes the sample to turn grayish-brown and strongly absorb visible light. Using Tauc plot relations, the band gaps of PCN, KPCN, and CoN/KPCN can be calculate to 2.93 eV, 2.83 eV, and 2.76 eV (Fig. 5b), respectively. KPCN and CoN/KPCN both exhibit smaller band gaps and stronger absorption of visible light (450–750 nm), especially CoN. Enhanced utilization of visible light is conducive to improved photocatalytic performance. The VB-XPS spectra (Fig. 5c) yield E_v values of 1.68 eV, 1.50 eV, and 1.39 eV for PCN, KPCN, and CoN/KPCN vs. NHE (Equation S1). Calculating $E_c = E_v - E_g$ (where E_c and E_v are the energy levels of CB and VB, E_g is the

band gap) gives E_c values of − 1.25 eV, − 1.32 eV, and − 1.37 eV vs. NHE for them (Table S3). A more negative conduction band (CB) position implies greater energy in excited electrons indicating a higher reduction capacity. This accounts for the excellent CO_2 reduction performance of CoN/KPCN.

To understand the interfacial charge transfer mechanism in CoN/KPCN, we calculated the work functions of KPCN and CoN using DFT calculations (Fig. 5d-e). The work functions (Φ) of KPCN and CoN were determined as 3.74 eV and 5.67 eV, respectively. It's apparent that the Fermi level of KPCN is higher than that of CoN, resulting in a band bending when they come into contact. Based on the above results, the band structures of KPCN and CoN can be expressed in Fig. 5f before, after contact and during light irradiation. Due to the inconsistency of Fermi levels, upon contact with KPCN, the Fermi level of CoN would bend upward while the KPCN would bend down. After contact, a hole accumulation region will be formed on the KPCN and an electron accumulation region on the CoN, which creates a built-in electric field between the CoN and the KPCN, consistent with the XPS results (Fig. 3c-e), facilitating the spontaneous transfer of electrons from KPCN to CoN. Under AM 1.5 G irradiation, photogenerated electrons first jump from the VB to the CB of KPCN and then transfer to CoN through the built-in electric field, leading to the CO_2 to CH_4 conversion on the surface of CoN. The built-in electric field enhances the transfer and utilization efficiency of photogenerated carriers in CoN/KPCN, whereas in PCN and KPCN, photogenerated electrons and holes tend to directly recombine. The PL spectra (Fig. S7) confirm that PCN, KPCN, and CoN/KPCN experience different recombination rates of photogenerated carriers, with lower recombination rates, CoN/KPCN suggests more efficient participation in the photocatalytic reaction.

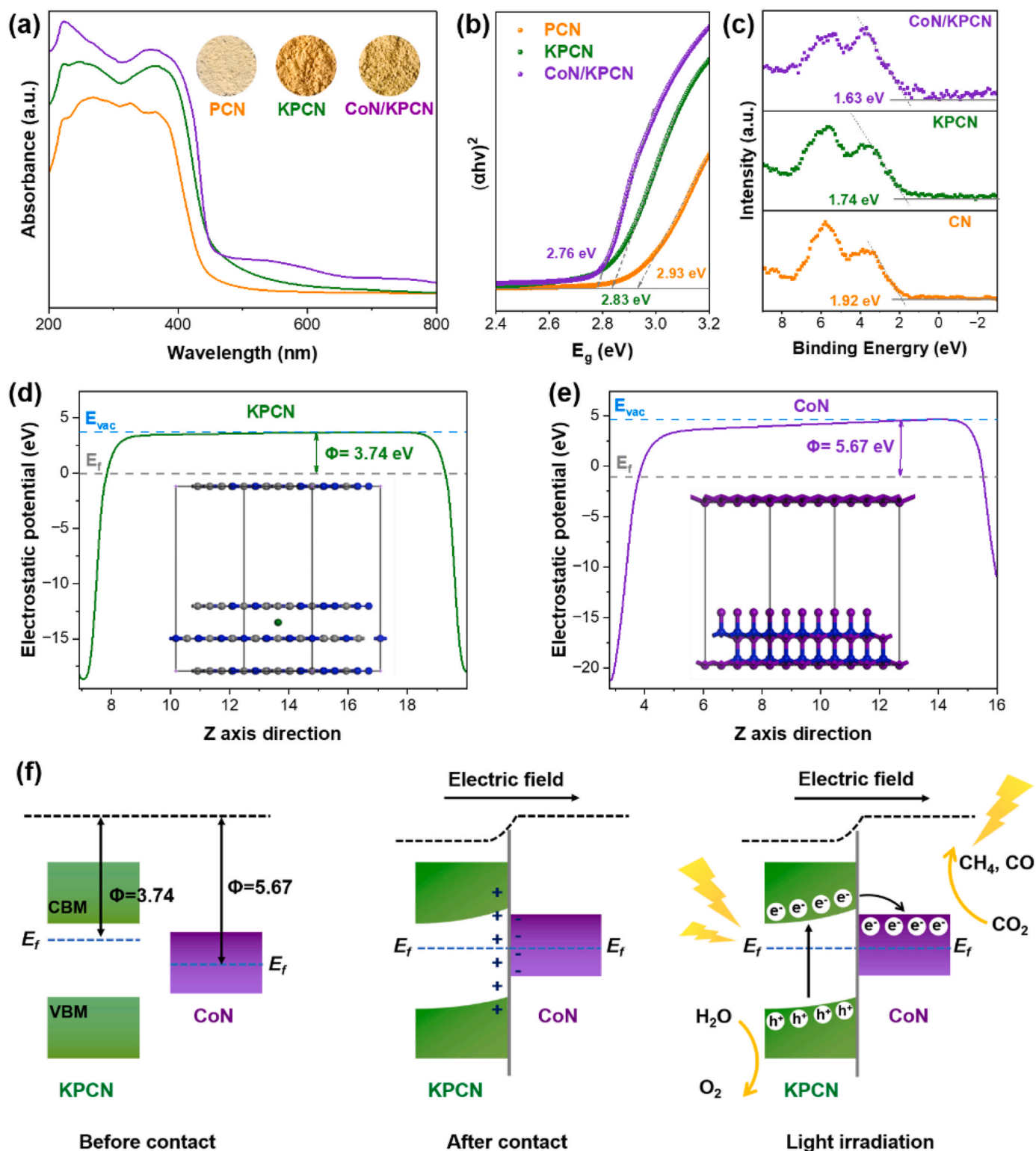Photoelectrochemical tests further assess the separation and transfer

Fig. 5. UV–vis diffuse reflectance spectra (a), Kubelka–Munk plot of the diffuse reflectance data (b) and VB-XPS spectra (c) of PCN, KPCN, and CoN/KPCN; Calculated work functions of (d) KPCN, (e) CoN; Schottky contact model of CoN/KPCN and its charge transfer mechanism.

efficiency of photogenerated carriers. The transient photocurrent of CoN/KPCN under simulated sunlight is significantly stronger than that of PCN and KPCN (Fig. 6a), indicating more efficient carrier mobility in CoN/KPCN. Moreover, the smaller arc radius of CoN/KPCN in electrochemical impedance spectroscopy (EIS, Fig. 6b) implies lower charge transfer resistance and faster interfacial charge transfer. Fig. 6c shows that CoN/KPCN has a higher carrier density of $(3.39 \times 10^{21}$ cm$^{-3})$ than

that of PCN $(1.70 \times 10^{21}$ cm$^{-3})$ and KPCN $(1.19 \times 10^{21}$ cm$^{-3})$ according to the Mott-Schottky diagram (Equation S2). A steeper slope for CoN/KPCN confirms faster carrier transfer kinetics. Time-resolved photoluminescence (TRPL) spectra (Fig. 6d) show that CoN/KPCN has a shorter average TRPL lifetime (τ_{ave}=1.04 ns) compared to PCN (τ_{ave}=4.18 ns) and KPCN (τ_{ave}=1.72 ns), further confirming the effective separation of photogenerated electrons and holes in CoN/KPCN
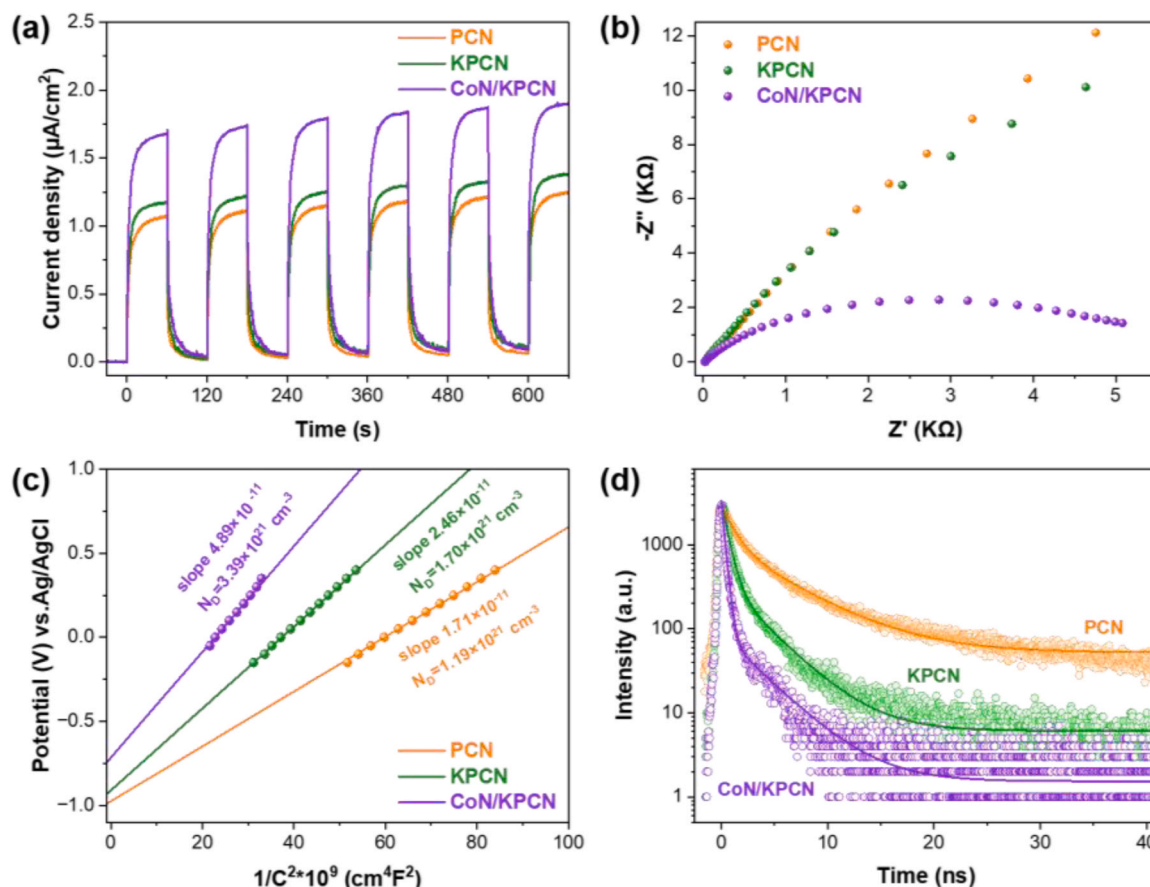
Fig. 6. Transient photocurrent spectra (a), EIS plots (b), linear fit plots of the linear parts of Mott-Schottky plots (c), TRPL spectra of PCN, KPCN, and CoN/KPCN.

[56], detailed decay values are displayed in Table S4.

Specific surface area and pore size distribution may also affect the catalytic performance, so we conducted Brunauer–Emmett–Teller (BET) tests on the PCN, KPCN, and CoN/KPCN. As shown in Fig. 7a, KPCN and CoN/KPCN exhibit significantly smaller specific surface areas compared to PCN due to K occupying interlayer cavities. However, the smaller specific surface area in CoN/KPCN, despite its excellent catalytic performance, suggests that the specific surface area is not the main factor influencing catalytic performance in this study. Pore size distributions (Fig. S8) indicate that mesopores around 10 nm dominate in PCN, KPCN, and CoN/KPCN. Considering that CO_2 adsorption is crucial for photocatalytic CO_2 reduction, we conducted CO_2 adsorption tests on the photocatalysts. CoN/KPCN exhibited much greater CO_2 adsorption capacity compared to PCN and KPCN (Fig. 7b), which provides a solid basis for subsequent CO_2 activation. DFT calculations further supported the adsorption capacity, as shown in Fig. 7c-d. The adsorption sites for CO_2 on PCN are the N atom connected to three C atoms in triazine with an adsorption energy of -0.07 eV. In contrast, the adsorption sites for CoN are Co atoms with an adsorption energy of -1.12 eV, 16 times higher than PCN. The electron cloud distribution cloud around CO_2 and the variation in CO_2 bond angles also indicate CO_2 adsorption strength. On the CoN (111) surface, the electron cloud around CO_2 is larger than that on PCN, indicating strong electron exchange between CO_2 and CoN. Additionally, the C═O bond angle of CO_2 on the CoN varies significantly, from the original 180.00° to 132.24°, while on the PCN surface, it remains essentially unchanged (179.69°). This substantial bond angle shift indicates effective CO_2 adsorption and activation on the CoN surface, benefiting photocatalytic reduction of CO_2 reaction.

3.4. Photocatalytic mechanism

To elucidate the shift in selectivity from CO to CH_4 in the photocatalytic reduction of CO_2 by CoN/KPCN, we employed in-situ diffuse reflectance Fourier transform infrared spectroscopy (DRIFTS) and Gibbs free energy calculations. During in-situ DRIFTS measurements, a continuous flow of CO_2 and H_2O was introduced in the dark for 15 min to allow fully adsorb CO_2 and H_2O on the catalyst. Then, we dynamically detected CO_2 intermediates on the catalysts during a 60 min illumination [57,58]. In-situ DRIFTS spectra of CoN/KPCN (Fig. S9a) revealed prominent intermediates in the photocatalytic reduction of CO_2. Peaks at 1541 cm^{-1}, 1699 cm^{-1} and 1338 cm^{-1}, 1648 cm^{-1} were attributed to monodentate carbonate (m-CO_3^{2-}) and bidentate carbonate (b-CO_3^{2-}), both of which signal the adsorption of CO_2. The O-C-O stretch at 1612 cm^{-1} is characteristic of b-CO_3^{2-} from adsorbed CO_2 [59]. Bidentate formate species (COO-) and carboxylate species (CO_2) observed at 1558 cm^{-1} and 1683 cm^{-1} are related to the intermediate product *COOH [58]. Additionally, a peak at 1717 cm^{-1} indicates C═O and slightly increase with light exposure, suggesting a small amount of CO production in CoN/KPCN during photocatalytic reaction [60]. Notably, the typical peaks of *CHO were observed at 1165 cm^{-1} and 1102 cm^{-1}, while peaks at 1063 cm^{-1} corresponded to *CH_3O, as shown in Fig. 8a and Fig. S9b, but these signals were absent in PCN (Fig. 8b). *CHO and *CH_3O are direct and indirect evidence of CO_2 photoreduction to CH_4 [61,62]. Specifically, *CHO results from the protonation of *CO, a key intermediate product in the photocatalytic reduction of CO_2 to CH_4, and *CH_3O is the direct indicator of CH_4 formation. Comparing the in-situ DRIFTS spectra of PCN with those of KPCN and CoN/KPCN, it is evident that PCN exhibits only CO signals, while KPCN and CoN/KPCN display both CO and CH_4 signals, consistent with the previously mentioned photocatalytic performance. The desorption of *CO to
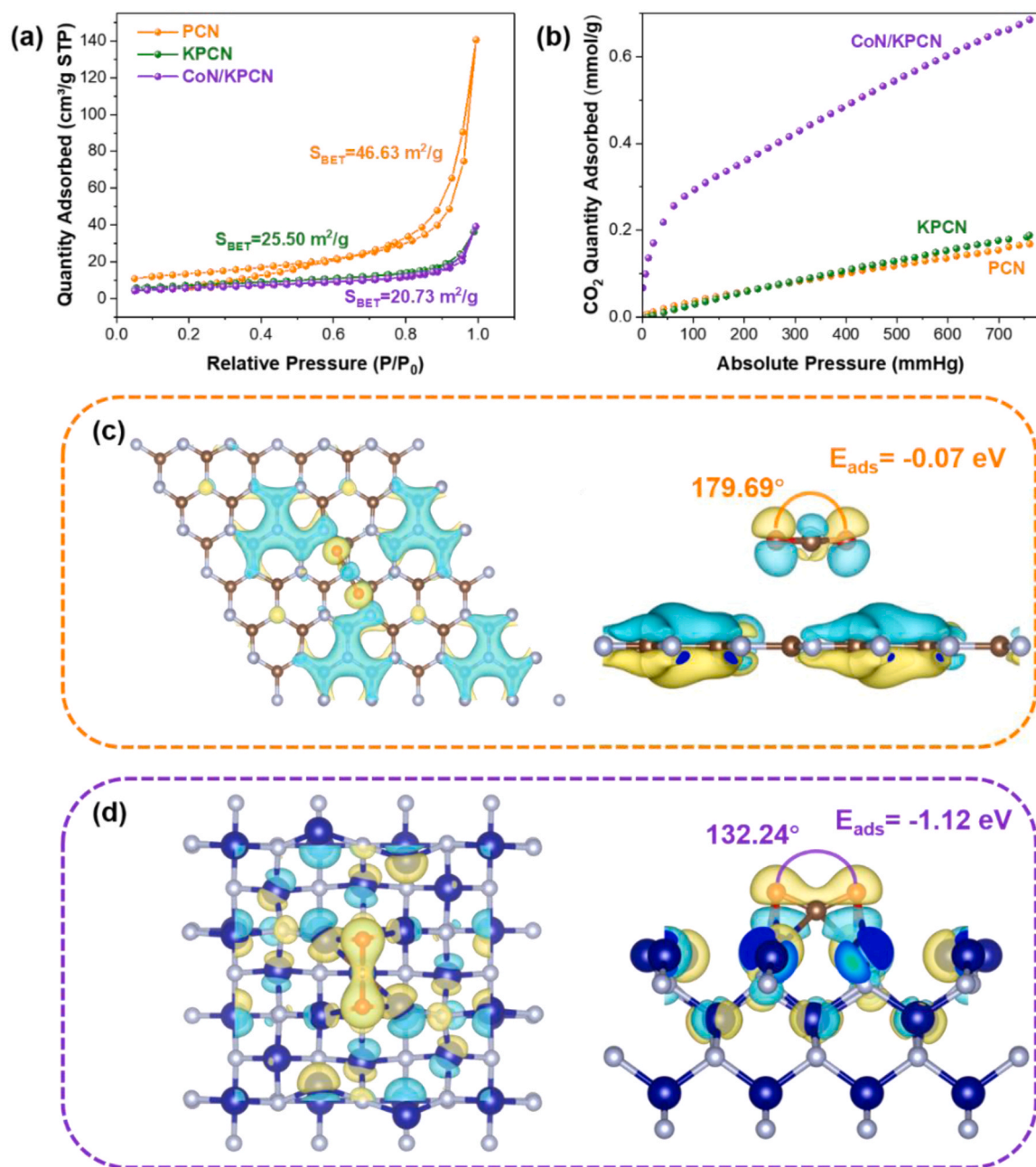
Fig. 7. N_2 adsorption/desorption isotherms (a), CO_2 adsorption isotherms (b) of PCN, KPCN, and CoN/KPCN; Optimized adsorption model and charge density difference of (c) PCN (0 0 1) and (d) CoN (1 1 1), top view (left), side view (right). The yellow/blue electron cloud indicates the accumulation/depletion of charge.

produce CO or protonation to form *CHO on the catalyst is a crucial step in determining the product type of CO_2 photoreduction.

To further support this point, we calculated the Gibbs free energy difference (Δ_G) for the desorption and protonation of *CO in PCN and KPCN using DFT calculations. We set the initial state as CO adsorbed on the catalyst (*CO), and the final state as gaseous CO and CHO adsorbed on the catalyst (*CHO). As known, lower energy barriers indicate easier reactions, and vice versa. Fig. 8c demonstrates that CO desorption has a Δ_G of -0.57 eV, making it easier than the protonation of *CO with a 1.60 eV Δ_G on PCN. For KPCN, both *CO desorption and protonation are spontaneous reactions, but the latter has a lower Gibbs free energy difference ($\Delta_G=-1.37$ eV). In other words, *CO is more likely to desorb directly to form gaseous CO on PCN, while on KPCN and CoN/KPCN, protonation is favored, generating *CHO, a key intermediate in CO_2 reduction to CH_4. DFT calculations have thermodynamically supported

the potential of KPCN and CoN/KPCN for realizing photocatalytic CO_2 to CH_4. Based on in-situ DRIFTS and DFT calculations, we propose an eight-electron reaction pathway for CO_2 photoreduction to CH_4 shown in Fig. 8d ($CO_2 \rightarrow {}^*CO_2 \rightarrow {}^*COOH \rightarrow {}^*CO \rightarrow {}^*CHO \rightarrow {}^*CH_3O \rightarrow CH_4$), where we simplify the repetitive protonation primitive reactions as detailed in Fig. S10. These reactions are represented as follows, where * represents catalysts, *CO_2, *COOH, *CO, *CHO, *CH_3O, *O, and *OH represents adsorbed CO_2, COOH, CO, CHO, and CH_3O, O, and OH.
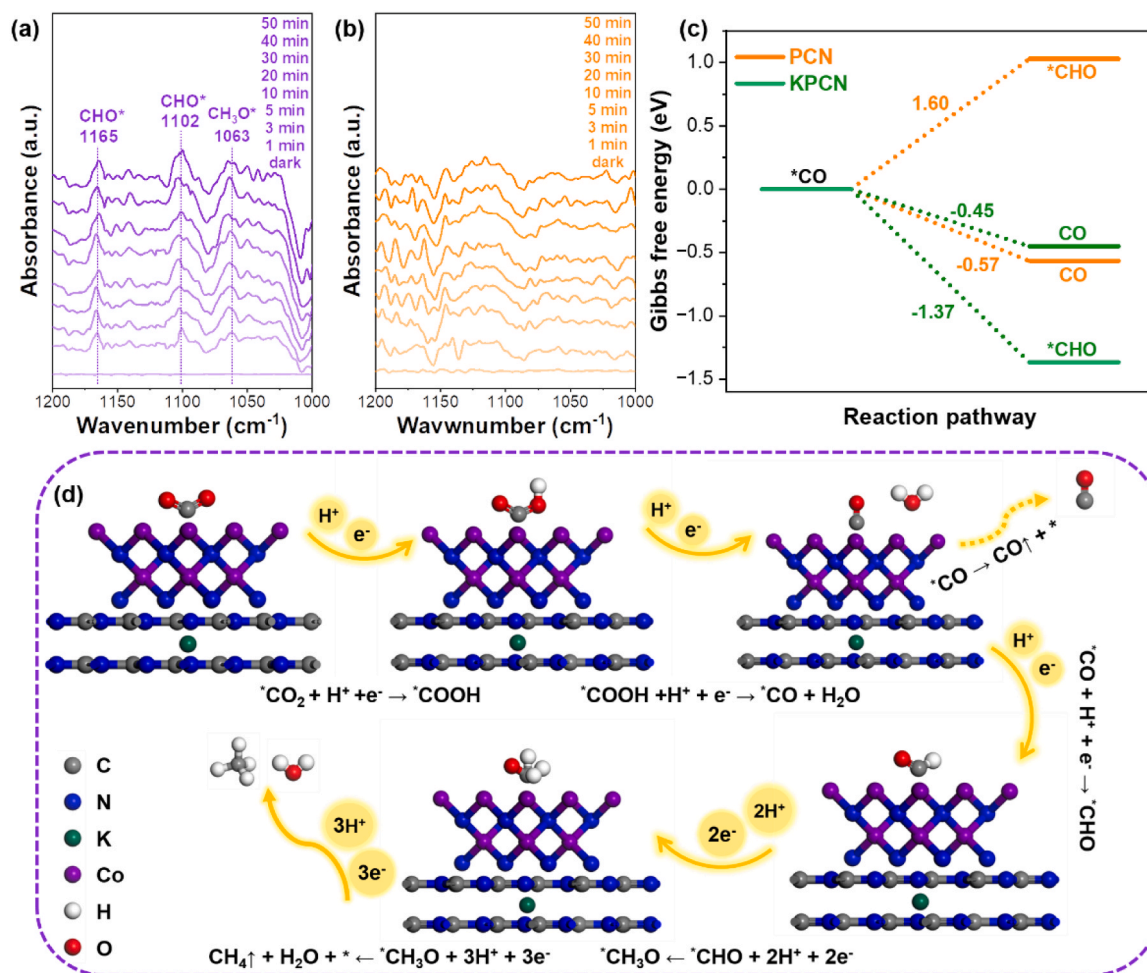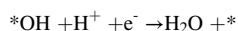
$$* + CO_2(g) \rightarrow {}^*CO_2 \tag{3}$$

$$^*CO_2 + H^+ + e^- \rightarrow {}^*COOH \tag{4}$$

$$^*COOH + H^+ + e^- \rightarrow {}^*CO + H_2O \tag{5}$$

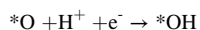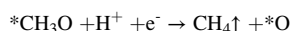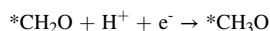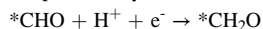$$^*CO + H^+ + e^- \rightarrow {}^*CHO \tag{6}$$

Fig. 8. In-situ DRIFTS spectra of CoN/KPCN (a) and PCN (b) over CO_2 +H_2O during photocatalytic reactions. Calculated Gibbs free energy (c) of PCN and KPCN for the photocatalytic CO_2 reduction process. Reaction path of photocatalytic reduction of CO_2 (d) over composite catalysts CoN/KPCN.

$$*CHO + H^+ + e^- \rightarrow *CH_2O \tag{7}$$

$$*CH_2O + H^+ + e^- \rightarrow *CH_3O \tag{8}$$

$$*CH_3O + H^+ + e^- \rightarrow CH_4\uparrow + *O \tag{9}$$

$$*O + H^+ + e^- \rightarrow *OH \tag{10}$$

$$*OH + H^+ + e^- \rightarrow H_2O + * \tag{11}$$

4. Conclusions

In this study, we rapidly and uniformly heated a molten salt (KBr) with microwaves to create an ion conductor, which led to the directional doping of K ions into the interlayer cavities of PCN for improving the crystallinity of PCN. Under microwave irradiation, ionic conductors promoted the selective formation of CoN nanoparticles on the surface of KPCN, resulting in the in-situ construction of the CoN/KPCN composite catalyst. This composite demonstrated a high yield of 45.71 μmol g^{-1} h^{-1} and selectivity of 98.18% in the photocatalytic reduction of CO_2 to CH_4, which were 36.0 and 2.1 times higher than those of PCN, respectively. XPS, UV-Vis and photoelectrochemical tests revealed that the enhanced photocatalytic performance of CoN/KPCN composite was attributed to broadened light absorption, improved charge transfer paths, increased carrier separation and transfer efficiency, and enhanced CO_2 adsorption capacity due to selective loading of CoN on KPCN. Furthermore, the introduction of K ions was shown to shift the selectivity of CO_2 photoreduction from CO to CH_4 both kinetically and

thermodynamically, as demonstrated by experiments and DFT calculations. In summary, this work presents novel insights into carbon nitride-based catalysts for the photocatalytic reduction of CO_2 and provides a rapid catalysts synthesis strategy via one-step microwave molten salt heating.

CRediT authorship contribution statement

Xiao Shuning: Conceptualization, Funding acquisition, Supervision, Writing – review & editing. **Li Guisheng:** Supervision. **Xue Yuhua:** Funding acquisition. **Fan Jinchen:** Writing – review & editing. **Song Xueling:** Writing – review & editing. **He Chengpeng:** Data curation, Writing – review & editing. **Shao Honglei:** Formal analysis, Software. **Qiu Suxin:** Data curation, Writing – original draft.

Declaration of Competing Interest

The authors declare no competing financial interest.

Data Availability

Data will be made available on request.

Appendix A. Supporting information

Supplementary data associated with this article can be found in the online version at doi:10.1016/j.apcatb.2023.123615.

References

[1] C. Wu, W. Huang, H. Liu, K. Lv, Q. Li, Appl. Catal. B Environ. 330 (2023), 122653.
[2] L. Lin, P. Lin, J. Song, Z. Zhang, X. Wang, W. Su, J. Colloid Interface Sci. 630 (2023) 352–362.
[3] P. Verma, S. Zhang, S. Song, K. Mori, Y. Kuwahara, M. Wen, H. Yamashita, T. An, J. CO_2 Util. 54 (2021), 101765.
[4] P. Zhang, H. Cheng, F. Gu, S. Hong, H. Dong, C. Li, Surf. Interfaces 42 (2023), 103368.
[5] Y. Wang, X. Shang, J. Shen, Z. Zhang, D. Wang, J. Lin, J.C.S. Wu, X. Fu, X. Wang, C. Li, Nat. Commun. 11 (2020) 3043.
[6] P. Zhang, S. Sui, Y. Wang, Z. Wang, J. Zhao, N. Wen, H. Chen, H. Huang, Z. Zhang, R. Yuan, Z. Ding, W. Dai, X. Fu, Y.X. Weng, J. Long, J. Am. Chem. Soc. 145 (2023) 5769–5777.
[7] Y. Wu, Y. Yang, M. Gu, C. Bie, H. Tan, B. Cheng, J. Xu, Chin. J. Catal. 53 (2023) 123–133.
[8] S. Song, Q. Liu, J. Xiong, M. Wen, T. An, J. Catal. 421 (2023) 77–87.
[9] M. Lv, S. Song, P. Verma, M. Wen, Catal. Today 410 (2023) 135–142.
[10] W. Ji, F. Yang, J. Sun, R. Xu, P. Li, L. Jing, ACS Appl. Mater. Interfaces 15 (2023) 11961–11969.
[11] X. Wu, H. Ma, K. Wang, J. Wang, G. Wang, H. Yu, J. Colloid Interface Sci. 633 (2023) 817–827.
[12] C. Li, N. Su, H. Wu, C. Liu, G. Che, H. Dong, Inorg. Chem. 61 (2022) 13453–13461.
[13] C. Li, P. Zhang, F. Gu, L. Tong, J. Jiang, Y. Zuo, H. Dong, Chem. Eng. J. 476 (2023), 146514.
[14] Y. Li, X. Pang, Q. Zhao, B. Zhang, X. Guo, Y. Zhang, Y. Xie, C. Qin, L. Jing, ACS Appl. Mater. Interfaces 15 (2023) 5365–5377.
[15] H. Zhang, P. Zhang, J. Zhao, Y. Liu, Y. Huang, H. Huang, C. Yang, Y. Zhao, K. Wu, X. Fu, S. Jin, Y. Hou, Z. Ding, R. Yuan, M.B.J. Roeffaers, S. Zhong, J. Long, Angew. Chem. Int. Ed. 60 (2021) 16009–16018.
[16] Y. Geng, D. Chen, N. Li, Q. Xu, H. Li, J. He, J. Lu, Appl. Catal. B Environ. 280 (2021), 119409.
[17] D. Qin, Y. Xia, Q. Li, C. Yang, Y. Qin, K. Lv, J. Mater. Sci. Technol. 56 (2020) 206–215.
[18] J. Fu, Q. Xu, J. Low, C. Jiang, J. Yu, Appl. Catal. B Environ. 243 (2019) 556–565.
[19] Y. Zhu, T. Wan, X. Wen, D. Chu, Y. Jiang, Appl. Catal. B Environ. 244 (2019) 814–822.
[20] S. Zhang, J. Guo, W. Zhang, H. Gao, J. Huang, G. Chen, X. Xu, ACS Sustain. Chem. Eng. 9 (2021) 11479–11492.
[21] S. Wu, C. He, L. Wang, J. Zhang, Chem. Eng. J. 443 (2022), 136425.
[22] P. Chen, K. Xu, Z. Fang, Y. Tong, J. Wu, X. Lu, X. Peng, H. Ding, C. Wu, Y. Xie, Angew. Chem. Int. Ed. 54 (2015) 14710–14714.
[23] Y. Zhang, B. Ouyang, J. Xu, G. Jia, S. Chen, R.S. Rawat, H.J. Fan, Angew. Chem. Int. Ed. 55 (2016) 8670–8674.
[24] J. Di, C. Chen, C. Zhu, P. Song, M. Duan, J. Xiong, R. Long, M. Xu, L. Kang, S. Guo, S. Chen, H. Chen, Z. Chi, Y.-X. Weng, H. Li, L. Song, M. Wu, Q. Yan, S. Li, Z. Liu, Nano Energy 79 (2021), 105429.
[25] H. Gong, X. Hao, H. Li, Z. Jin, J. Colloid Interface Sci. 585 (2021) 217–228.
[26] B. Zhao, D. Gao, Y. Liu, J. Fan, H. Yu, J. Colloid Interface Sci. 608 (2022) 1268–1277.
[27] K. Wang, G. Gu, S. Hu, J. Zhang, X. Sun, F. Wang, P. Li, Y. Zhao, Z. Fan, X. Zou, Chem. Eng. J. 368 (2019) 896–904.
[28] L. Tian, J. Li, F. Liang, S. Chang, H. Zhang, M. Zhang, S. Zhang, J. Colloid Interface Sci. 536 (2019) 664–672.
[29] Z. Sun, H. Dong, Q. Yuan, Y. Tan, W. Wang, Y. Jiang, J. Wan, J. Wen, J. Yang, J. He, T. Cheng, L. Huang, Chem. Eng. J. 435 (2022), 134865.
[30] T. Xiong, W. Cen, Y. Zhang, F. Dong, ACS Catal. 6 (2016) 2462–2472.
[31] Y. Xu, C. Qiu, X. Fan, Y. Xiao, G. Zhang, K. Yu, H. Ju, X. Ling, Y. Zhu, C. Su, Appl. Catal. B Environ. 268 (2020), 118457.
[32] G. Zhang, Y. Xu, D. Yan, C. He, Y. Li, X. Ren, P. Zhang, H. Mi, ACS Catal. 11 (2021) 6995–7005.
[33] J. Sun, Y. Guan, G. Yang, S. Qiu, H. Shao, Y. Wang, G. Li, S. Xiao, ACS Sustain. Chem. Eng. 11 (2023) 14827–14840.
[34] Y. Sun, S. Qiu, Z. Fang, J. Yang, X. Song, S. Xiao, ACS Sustain. Chem. Eng. 11 (2023) 3359–3369.
[35] S. Xiao, M. Huo, Y. Guan, H. Cao, Q. Huang, L. Chen, S. Li, G. Li, D. Zhang, H. Li, Small Struct. 3 (2022) 2100169.
[36] Y. Liu, X. Guo, Z. Chen, W. Zhang, Y. Wang, Y. Zheng, X. Tang, M. Zhang, Z. Peng, R. Li, Y. Huang, Appl. Catal. B Environ. 266 (2020), 118624.
[37] H. Zhang, W.Y. Noh, F. Li, J.H. Kim, H.Y. Jeong, J.S. Lee, Adv. Funct. Mater. 29 (2019) 1805737.
[38] Y.J. Zhu, F. Chen, Chem. Rev. 114 (2014) 6462–6555.
[39] Y.-P. Yuan, L.-S. Yin, S.-W. Cao, L.-N. Gu, G.-S. Xu, P. Du, H. Chai, Y.-S. Liao, C. Xue, Green. Chem. 16 (2014) 4663–4668.
[40] J. Robinson, S. Kingman, D. Irvine, P. Licence, A. Smith, G. Dimitrakis, D. Obermayer, C.O. Kappe, Phys. Chem. Chem. Phys. 12 (2010) 4750–4758.
[41] H. Liu, D. Chen, Z. Wang, H. Jing, R. Zhang, Appl. Catal. B Environ. 203 (2017) 300–313.
[42] Y. Sun, X. Zhao, X. Song, J. Fan, J. Yang, Y. Miao, S. Xiao, J. Environ. Sci. 138 (2024) 671–683, https://doi.org/10.1016/j.jes.2023.04.023.
[43] G. Kresse, J. Furthmüller, Phys. Rev. B. 54 (1996) 11169.
[44] J.P. Perdew, K. Burke, M. Ernzerhof, Phys. Rev. Lett. 77 (1996) 3865.
[45] W. Zhang, X. Xiao, Y. Li, X. Zeng, L. Zheng, C. Wan, Appl. Surf. Sci. 389 (2016) 496–506.
[46] Y. Wang, S. Zhao, Y. Zhang, J. Fang, Y. Zhou, S. Yuan, C. Zhang, W. Chen, Appl. Surf. Sci. 440 (2018) 258–265.
[47] J. Zhang, G. Zhang, J. Zhang, Appl. Surf. Sci. 475 (2019) 256–263.
[48] K. Wang, J. Fu, Y. Zheng, Appl. Catal. B Environ. 254 (2019) 270–282.
[49] Y. Xu, X. He, H. Zhong, D.J. Singh, L. Zhang, R. Wang, Appl. Catal. B Environ. 246 (2019) 349–355.
[50] S. Yan, Y. Li, X. Yang, X. Jia, J. Xu, H. Song, Adv. Mater. (2023) 2307967.
[51] G. Zhang, J. Zhu, Y. Xu, C. Yang, C. He, P. Zhang, Y. Li, X. Ren, H. Mi, ACS Catal. 12 (2022) 4648–4658.
[52] C. Qiu, Y. Xu, X. Fan, D. Xu, R. Tandiana, X. Ling, Y. Jiang, C. Liu, L. Yu, W. Chen, C. Su, Adv. Sci. 6 (2019) 1801403.
[53] W. Yuan, S. Wang, Y. Ma, Y. Qiu, Y. An, L. Cheng, ACS Energy Lett. 5 (2020) 692–700.
[54] Z. Jin, T. Wei, L. Lixue, F. Li, R. Tao, L. Xu, Dalton Trans. 48 (2019) 2676–2682.
[55] D. Zhao, C.L. Dong, B. Wang, C. Chen, Y.C. Huang, Z. Diao, S. Li, L. Guo, S. Shen, Adv. Mater. 31 (2019) 1903545.
[56] S. Xiao, Y. Guan, H. Shang, H. Li, Z. Tian, S. Liu, W. Chen, J. Yang, J. CO_2 Util. 55 (2022), 101806.
[57] R. Chong, Y. Fan, Y. Du, L. Liu, Z. Chang, D. Li, Int. J. Hydrog. Energy 43 (2018) 22329–22339.
[58] D. Xu, B. Cheng, W. Wang, C. Jiang, J. Yu, Appl. Catal. B Environ. 231 (2018) 368–380.
[59] X. Li, Y. Sun, J. Xu, Y. Shao, J. Wu, X. Xu, Y. Pan, H. Ju, J. Zhu, Y. Xie, Nat. Energy 4 (2019) 690–699.
[60] J. Di, C. Zhu, M. Ji, M. Duan, R. Long, C. Yan, K. Gu, J. Xiong, Y. She, J. Xia, H. Li, Z. Liu, Engl. Angew. Chem. Int. Ed. 57 (2018) 14847–14851.
[61] L. Jiang, K. Wang, X. Wu, G. Zhang, Sol. Rrl. 5 (2020), 2000326.
[62] L. Cheng, X. Yue, J. Fan, Q. Xiang, Adv. Mater. 34 (2022) 2200929.